Supporting Information

Oriented Assembly of Anisotropic Nanosheets into Ultrathin Flowerlike Superstructures for Energy Storage

Jingjing Cao[1], Tianpeng, Zhou[1], Yunlong Xu[1], Yunbiao Qi[1], Wei Jiang[1], Wei Wang*[2], Ping Sun[1], Aimin Li[1] and Quanxing Zhang[1]*

[1] State Key Laboratory of Pollution Control and Resources Reuse, School of the Environment, Nanjing University, Nanjing, 210023, China.

[2] Department of Chemistry and Centre for Pharmacy, University of Bergen, Bergen, 5007, Norway.

E-mail: jiangwei@nju.edu.cn (W.J.); wei.wang@uib.no (W.W.)

Figure Captions in Supporting Information

Figure S1. EDS and mapping analysis of $CoNi_2$-OH/L-Asn. (a−d) EDS mapping of Co, Ni and Cl element, and (e) EDS of $CoNi_2$-OH/L-Asn.

Figure S2. TGA analysis of $CoNi_2$-OH/L-Asn

Figure S3. SEM images of the Co_xNi_{2-x}-OH/L-Asn at different Co: Ni feed ratio. (a) $CoNi_2$-OH/L-Asn, (b) CoNi-OH/L-Asn and (c) Co_2Ni-OH/ L-Asn.

Figure S4. SEM images of the $CoNi_2$-OH at different LAs. (a-i) $CoNi_2$-OH/L-Glu, $CoNi_2$-OH/L-Asp, $CoNi_2$-OH/L-Asn, $CoNi_2$-OH/L-Phe, $CoNi_2$-OH/L-Met and $CoNi_2$-OH/L-Ser, $CoNi_2$-OH/L-Arg, $CoNi_2$-OH/L-Lys and $CoNi_2$-OH/L-His, respectively.

Figure S5. XRD analysis of $CoNi_2$-OH and $CoNi_2$-OH/L-Asn. (a) XRD patterns of the $CoNi_2$-OH, Co_xNi_{2-x}-OH/L-Asn. (b) XRD patterns of the CoNi2-OH/L-Asn during synthesis at room temperature. (c) XRD patterns of $CoNi_2$-OH/L-Asn at different reaction times.

Figure S6. XPS analysis of $CoNi_2$-OH and $CoNi_2$-OH/L-Asn. XPS spectra of (a, b) Cl 2p.

Figure S7. Nitrogen sorption results. Nitrogen adsorption−desorption isotherm and pore size distribution analysis of $CoNi_2$-OH, $CoNi_2$-OH/L-Asn.

Table 1. Surface area and pore volume results of $CoNi_2$-OH, $CoNi_2$-OH/L-Asn.

Figure S8. Redox reactions of the Co_xNi_{2-x}-OH/L-Asn electrodes.

Figure S9. Cyclic voltammetry curves of Co_2Ni-OH/L-Asn, CoNi-OH/L-Asn, and $CoNi_2$-OH. (a-c) CV curves at the different scan rates.

Figure S10. Cyclic voltammetry curves of Co-OH/L-Asn, Ni-OH/L-Asn. (a, b) CV curves at the different scan rates.

Figure S11. Cyclic voltammetry curves and galvanostatic discharge curves of $CoNi_2$-OH/L-Glu, $CoNi_2$-OH/L-Asp. (a, c) CV curves at the different scan rates, and (b, d) GCD curves at the different current densities.

Figure S12. Cyclic voltammetry curves and galvanostatic discharge curves of $CoNi_2$-OH/L-Phe, $CoNi_2$-OH/L-Met and $CoNi_2$-OH/L-Ser. (a, c, e) CV curves at different scan rates, and (b, d, f) GCD curves at different current densities.

Figure S13. Cyclic voltammetry curves and galvanostatic discharge curves of $CoNi_2$-OH/L-Arg, $CoNi_2$-OH/L-His and $CoNi_2$-OH/L-Lys. (a, c, e) CV curves at different scan rates, respectively, and (b, d, f) GCD curves at different current densities.

Figure S14. Capacitive and diffusion-controlled contributions to charge storage. (a) CV curves of $CoNi_2$-OH/L-Asn at different scan rates. b) The plots of log(i) against log(v) for $CoNi_2$-OH/L-Asn. c) Separation of

the capacitive and diffusion-controlled currents of $CoNi_2$-OH/L-Asn electrode at a scan rate of 5 mV s^{-1}. d) Relative contributions of the capacitive and diffusion-controlled charge storage processes at different scan rates.

Figure S15. Nyquist plots of Co_xNi_{2-x}-OH/L-Asn electrodes.

Figure S16. Cyclic voltammetry curves and galvanostatic discharge curves of N-rGO. (a) CV curves, (b) GCD curves

Figure S17. (a) CV curves for $CoNi_2$-OH/L-Asn and N-rGO. (b) CV curves of the $CoNi_2$-OH/L-Asn//N-rGO device obtained in different potential windows.

Figure S18. The specific capacity values of the $CoNi_2$-OH/L-Asn//N-rGO devices at different current densities.

Figure S19. The TEM images of the electrode materials after 3000 cycles.

Table S2. Comparison of the electrochemical performance of ultrathin $CoNi_2$-OH/L-Asn electrode materials with the values in recent literature.

Table S3. The electrochemical cycling stability of the asymmetric supercapacitors based on the $CoNi_2$-OH/L-Asn//N-rGO devices for recently reported ASC.

Table S4. Comparison of the energy density and power density of ultrathin $CoNi_2$-OH/L-Asn electrode with the values reported in recent literature.

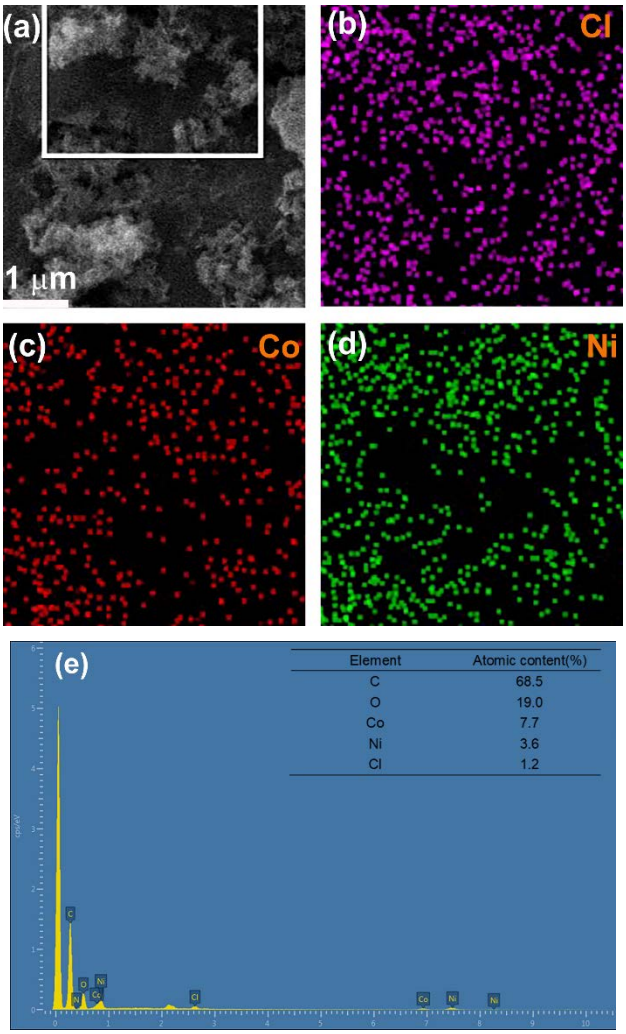

Figure S1. EDS and mapping analysis of $CoNi_2$-OH/L-Asn. (a−d) EDS mapping of Co, Ni and Cl element, and (e) EDS of $CoNi_2$-OH/L-Asn.

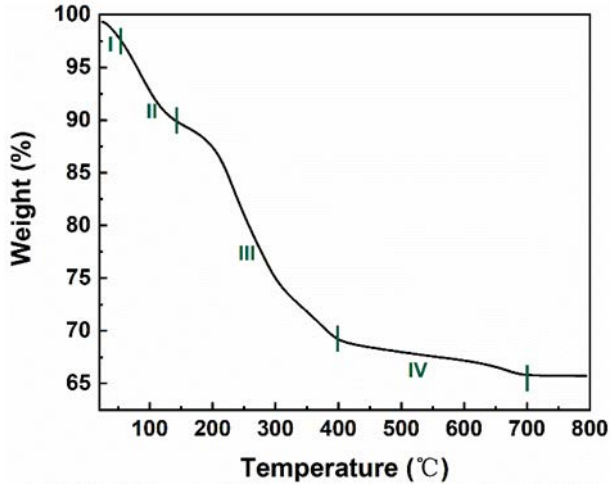

Figure S2. TGA analysis of $CoNi_2$-OH/L-Asn

The TG curve of the $CoNi_2$-OH/L-Asn sample in the temperature range of 25-800 °C (see figure below). The analysis of the TGA curve is based on a previous publication.[1]The $CoNi_2$-OH/L-Asn underwent weight loss of 33.7% in four steps indicated by the zones I, II, III, and

IV on the graph. The weight loss below 50 °C (stage I) is ascribed to the removal of the adsorbed water. The weight loss (9.54%) between 50 and 145 °C (stage II) is assigned to the evaporation of the intercalated water molecules. The weight loss (20.36%) ranging from 145 to 400 °C (stage III) is associated with the loss of water molecules produced by dehydroxylation of the hydroxide layers combined with the partial loss of Cl^{-}. Finally, the stage IV ending at about 700 °C can be attributed to the loss of Cl^{-} ions. Therefore, the composition of the as-prepared $CoNi_2$-OH/L-Asn sample was estimated to be $CoNi_2(OH)_{4.05}Cl_{0.34}\cdot 1.79H_2O$ (Co, 20.3%; Ni, 40.53%; OH^{-}, 23.77%; Cl^{-}, 4.19%; H_2O, 11.14%;). The predominant anionic species in the interlayer of the $CoNi_2$-OH/L-Asn sample was Cl^{-} ions, which were accommodated in the interlayer together with water molecules.

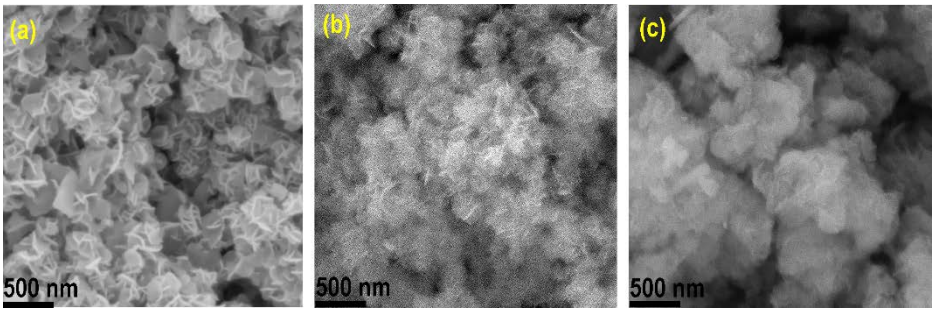

Figure S3. SEM images of the Co_xNi_{2-x}-OH/L-Asn at different Co: Ni feed ratio. (a) $CoNi_2$-OH/L-Asn, (b) CoNi-OH/L-Asn and (c) Co_2Ni-OH/L-Asn.

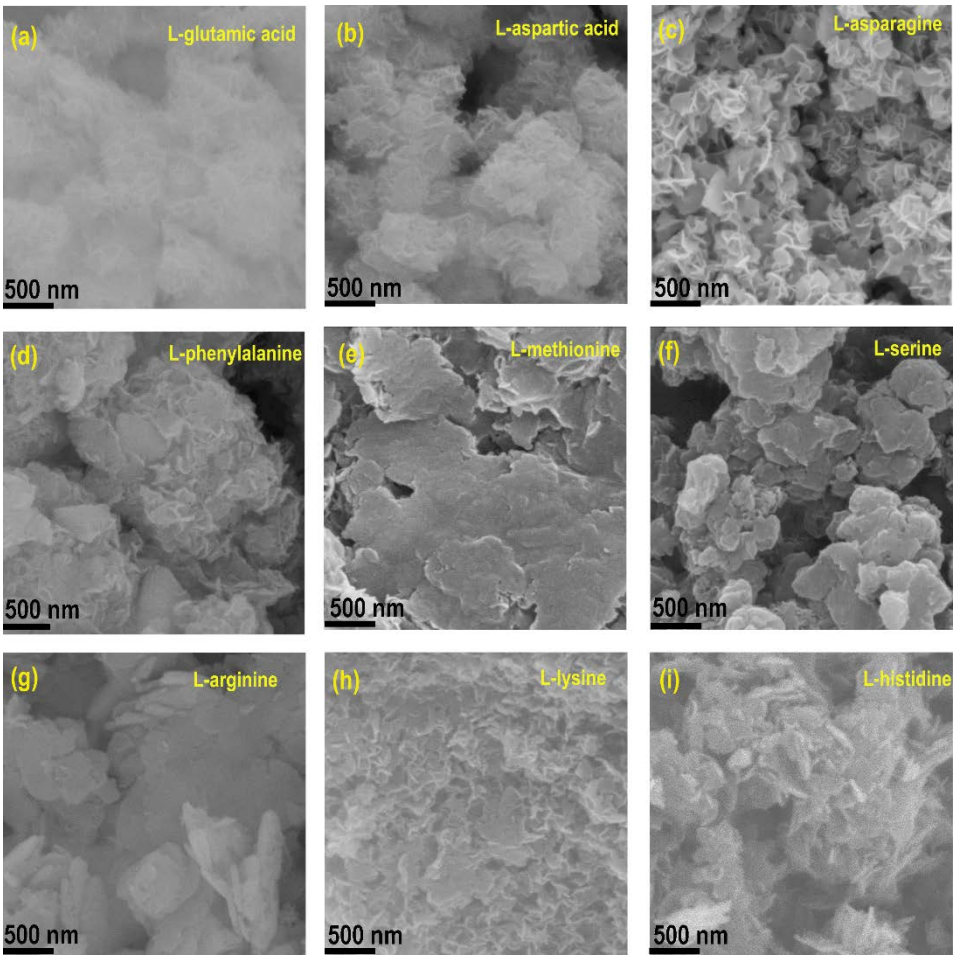

Figure S4. SEM images of the $CoNi_2$-OH at different LAs. (a-i) $CoNi_2$-OH/L-Glu, $CoNi_2$-OH/L-Asp, $CoNi_2$-OH/L-Asn, $CoNi_2$-OH/L-Phe, $CoNi_2$-OH/L-Met and $CoNi_2$-OH/L-Ser, $CoNi_2$-OH/L-Arg, $CoNi_2$-OH/L-Lys and $CoNi_2$-OH/L-His, respectively.

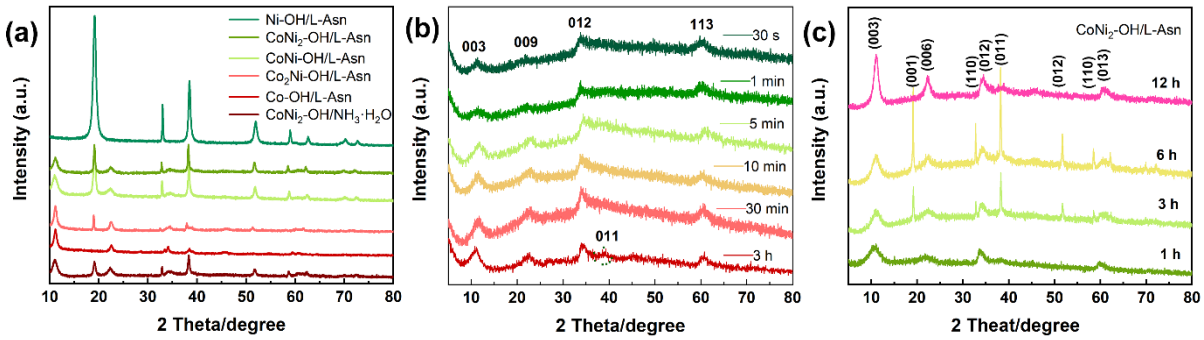

Figure S5. XRD analysis of $CoNi_2$-OH and $CoNi_2$-OH/L-Asn. (a) XRD patterns of the $CoNi_2$-OH, Co_xNi_{2-x}-OH/L-Asn. (b) XRD patterns of the CoNi2-OH/L-Asn during synthesis at room temperature. (c) XRD patterns of $CoNi_2$-OH/L-Asn at different reaction times.

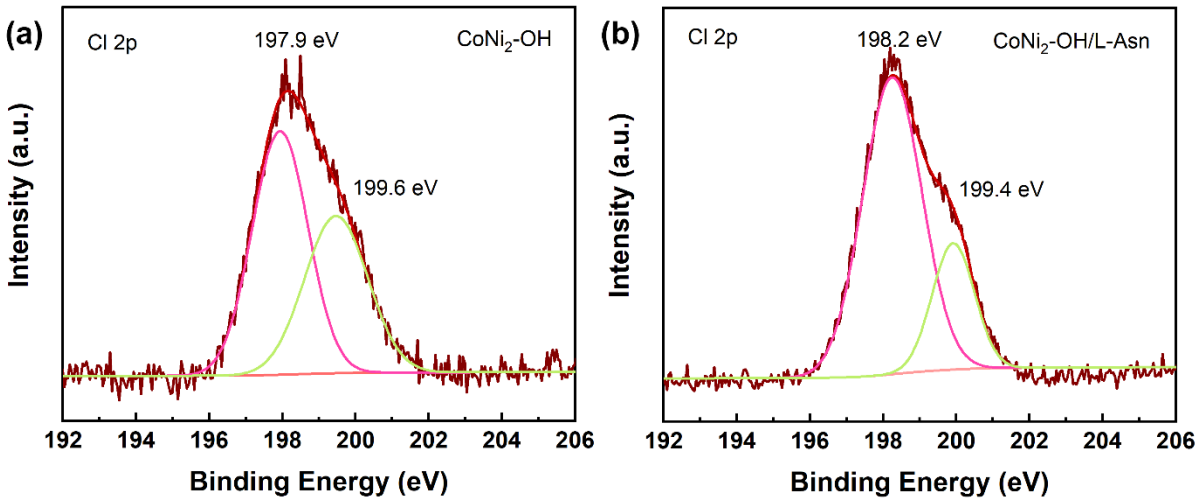

Figure S6. XPS analysis of $CoNi_2$-OH and $CoNi_2$-OH/L-Asn. XPS spectra of (a, b) Cl 2p.

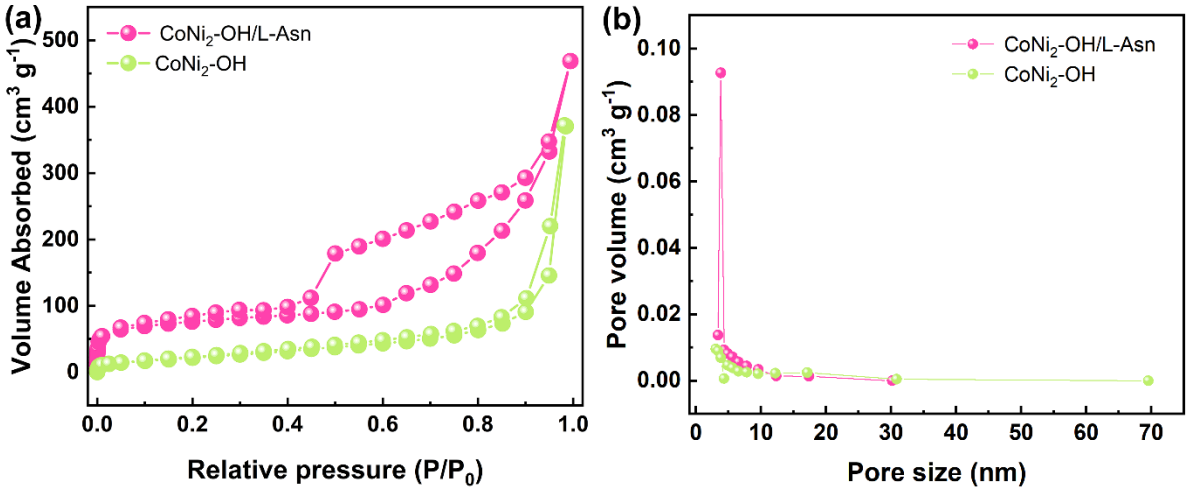

Figure S7. Nitrogen sorption results. Nitrogen adsorption−desorption isotherm and pore size distribution analysis of $CoNi_2$-OH, $CoNi_2$-OH/L-Asn

Table 1. Surface area and pore volume results of $CoNi_2$-OH, $CoNi_2$-OH/L-Asn.

Entry	Surface area ($cm^3\ g^{-1}$)	Pore volume ($cm^3\ g^{-1}$)
$CoNi_2$-OH	83.3	0.7247
CoNi2-OH/L-Asn	238.3	0.417

The redox reaction of Co_xNi_{2-x}-OH/L-Asn:[2]

$$Ni(OH)_2 + OH^- = NiOOH + H_2O + e^-$$

$$Co(OH)_2 + OH^- = CoOOH + H_2O + e^-$$

$$CoOOH + OH^- = CoO_2 + H_2O + e^-$$

Figure S8. Redox reactions of the Co_xNi_{2-x}-OH/L-Asn electrodes.

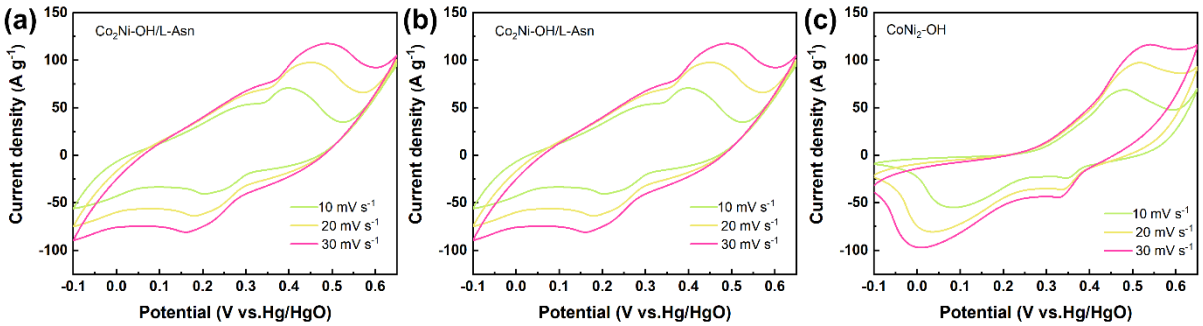

Figure S9. Cyclic voltammetry curves of Co_2Ni-OH/L-Asn, CoNi-OH/L-Asn, and $CoNi_2$-OH. (a-c) CV curves at the different scan rates.

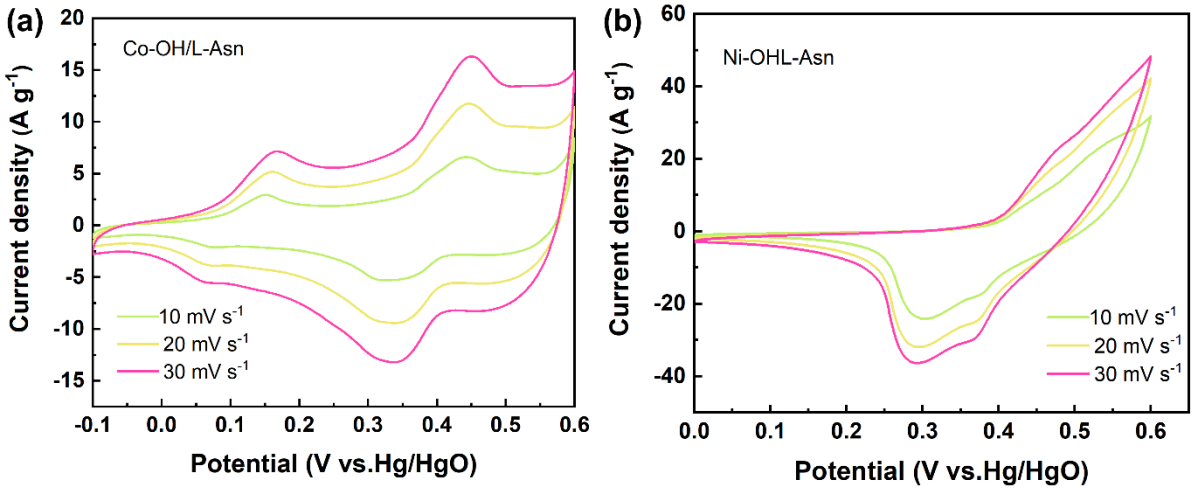

Figure S10. Cyclic voltammetry curves of Co-OH/L-Asn, Ni-OH/L-Asn. (a, b) CV curves at the different scan rates.

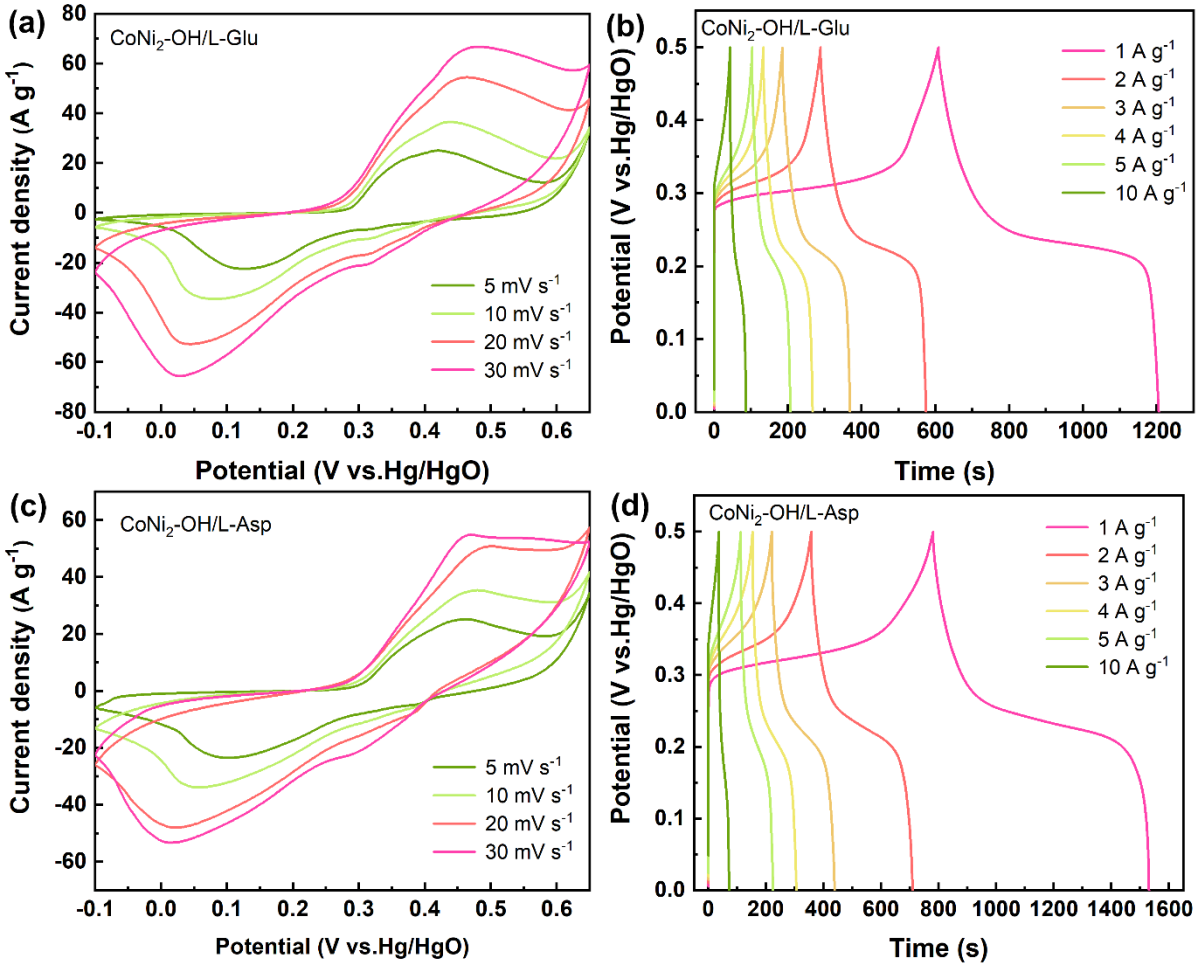

Figure S11. Cyclic voltammetry curves and galvanostatic discharge curves of $CoNi_2$-OH/L-Glu, $CoNi_2$-OH/L-Asp. (a, c) CV curves at the different scan rates, and (b, d) GCD curves at the different current densities.

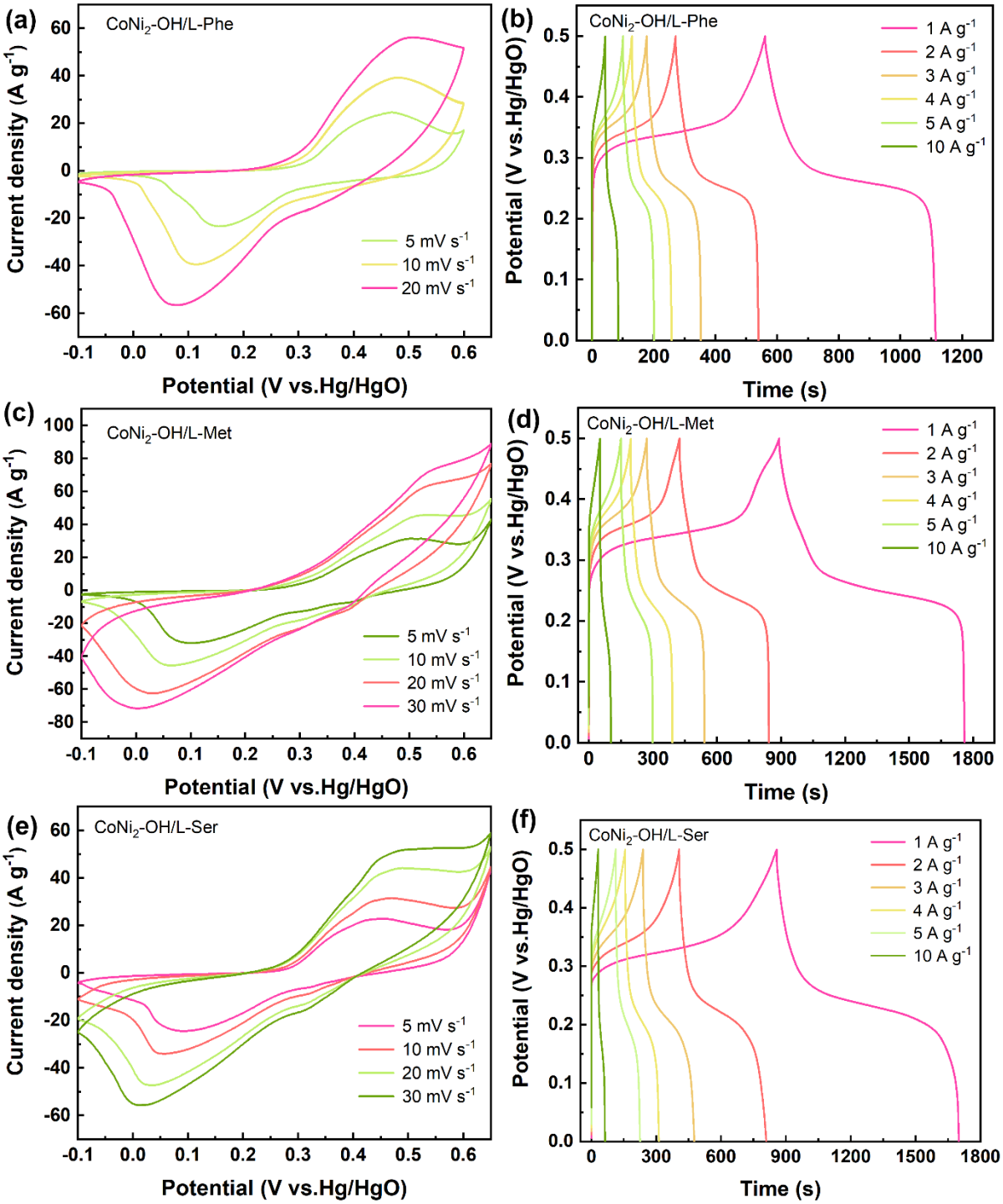

Figure S12. Cyclic voltammetry curves and galvanostatic discharge curves of $CoNi_2$-OH/L-Phe, $CoNi_2$-OH/L-Met and $CoNi_2$-OH/L-Ser. (a, c, e) CV curves at different scan rates, and (b, d, f) GCD curves at different current densities.

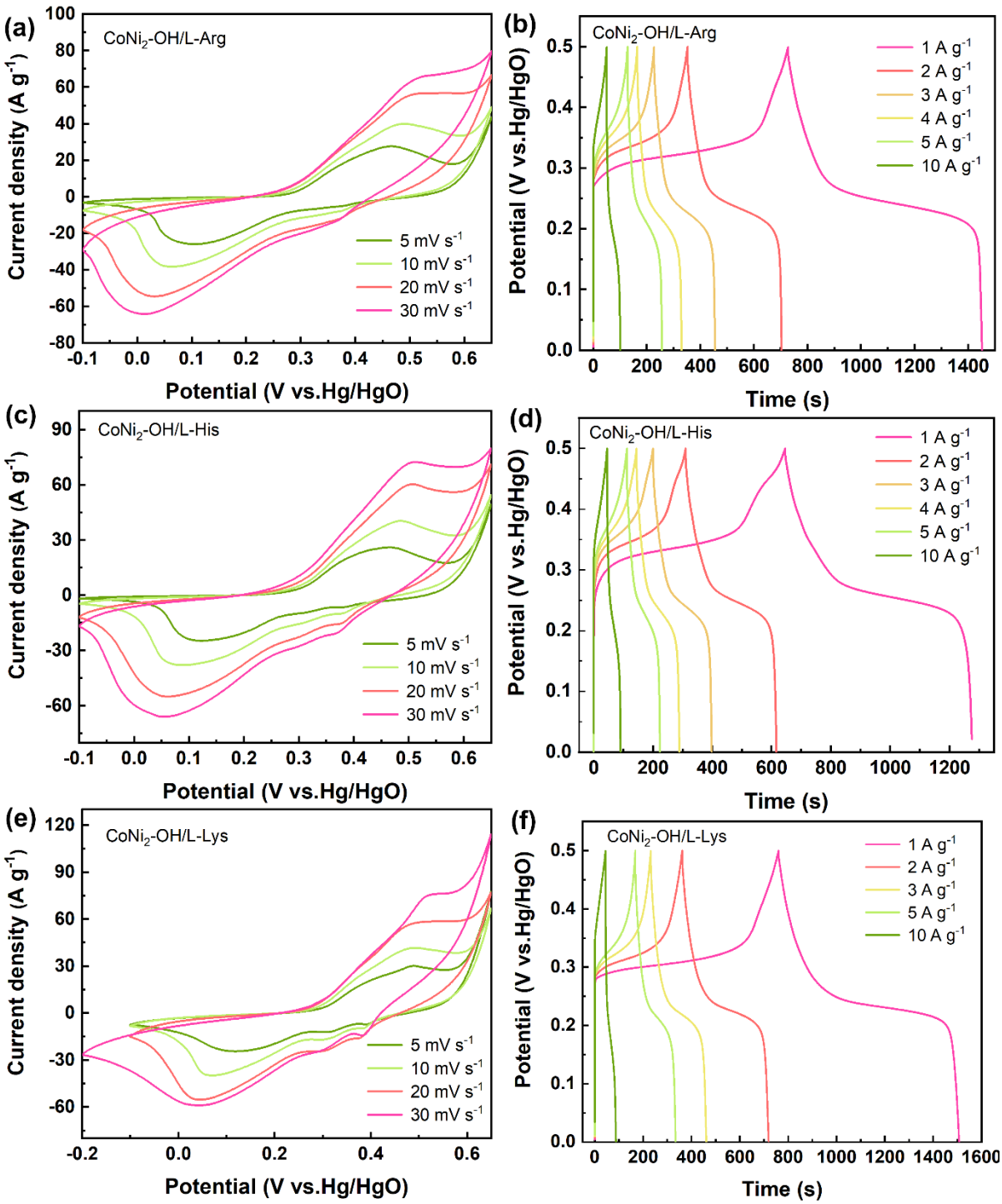

Figure S13. Cyclic voltammetry curves and galvanostatic discharge curves of $CoNi_2$-OH/L-Arg, $CoNi_2$-OH/L-His and $CoNi_2$-OH/L-Lys. (a, c, e) CV curves at different scan rates, respectively, and (b, d, f) GCD curves at different current densities.

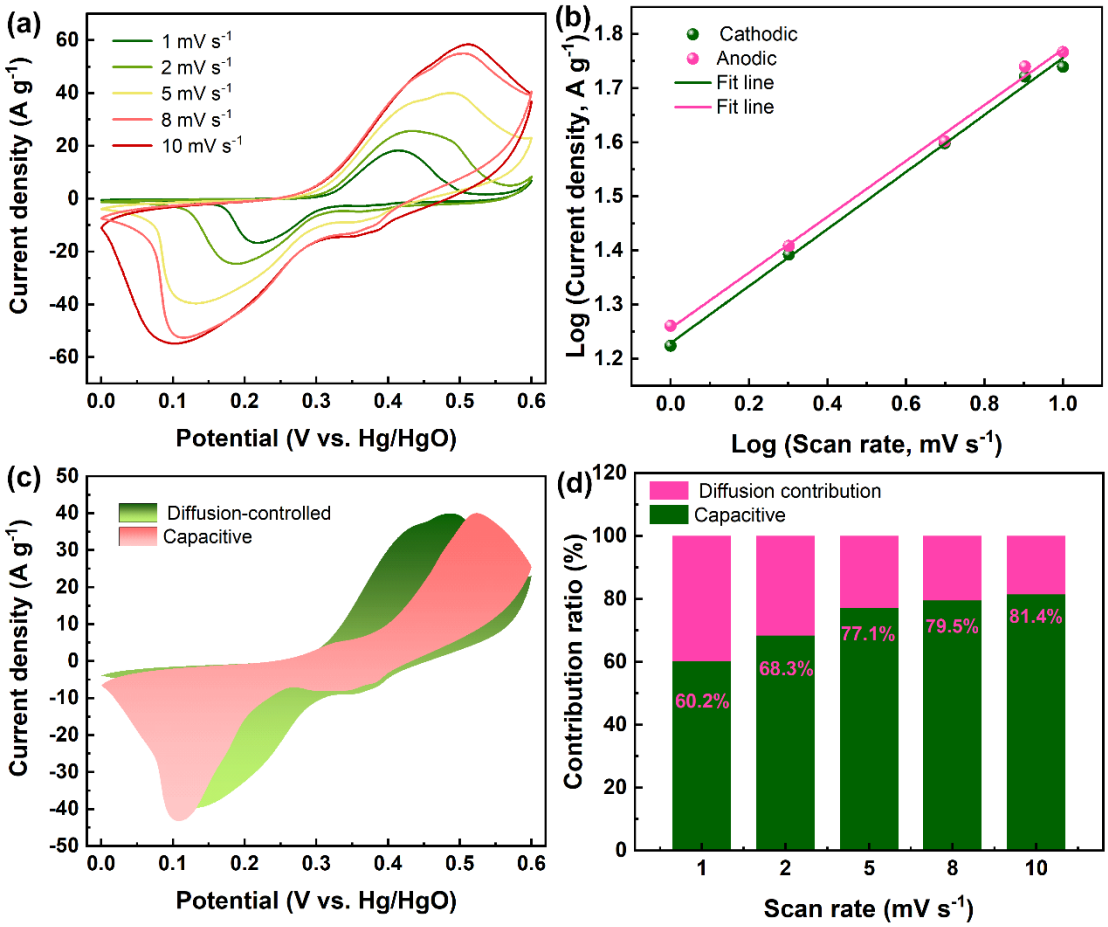

Figure S14. Capacitive and diffusion-controlled contributions to charge storage. (a) CV curves of $CoNi_2$-OH/L-Asn at different scan rates. b) The plots of log(i) against log(v) for $CoNi_2$-OH/L-Asn. c) Separation of the capacitive and diffusion-controlled currents of $CoNi_2$-OH/L-Asn electrode at a scan rate of 5 mV s^{-1}. d) Relative contributions of the capacitive and diffusion-controlled charge storage processes at different scan rates.

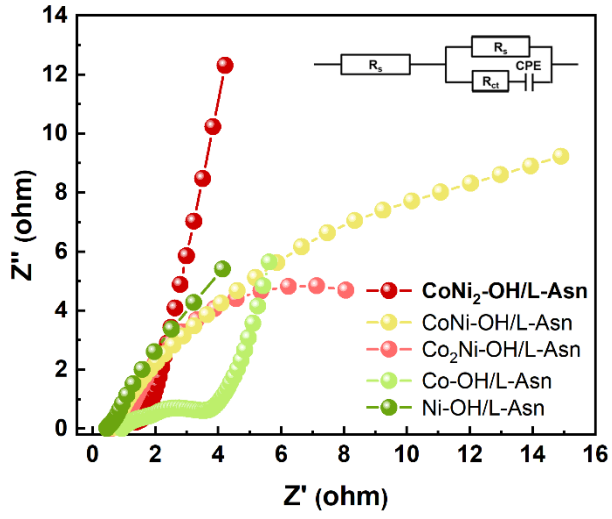

Figure S15. Nyquist plots of Co_xNi_{2-x}-OH/L-Asn electrodes.

We used electrochemical impedance spectroscopy (EIS) to evaluate the electrochemical performance

of the Co_xNi_{2-x}-OH/L-Asn electrodes (Fig. S15). The EIS cures show characteristic impedance semicircle of the transmission process in the high frequencies (HFs) zone and the characteristic straight line of the diffusion in the low-frequency zone. The Warburg impedance is caused by the polarization of the concentration difference. The inset image in Fig. S15 shows the equivalent circuit. The Nyquist plots obtained the intersection point of the semicircle of HFs on the real axis represents the series resistance (Rs) of the equivalent circuit, which mainly includes the intrinsic resistance and diffusion resistance of the active materials and the charge transfer resistance with the electrolyte. The diameter of the semicircle in the high-frequency region was ascribed to the charge-transfer resistance (Rct) linked to the exchanged current as defined in the Butler–Volmer equation. Real electrodes behave slightly more complex because of dispersion factors. These factors are mainly due to geometric aspects, such as electrode porosity and electrode roughness, especially for pseudocapacitors, active sites, and activation energy dispersion. Such fractal electrodes induce frequency dispersions of the electrical parameters. It is not accurate to simply consider the equivalent electrode interface dual-layer to a pure capacitor. To represent the electrical dispersions occurring in a real electrode, we used the constant phase element (CPE) introduced into the equivalent circuit. Fig. S15 demonstrates the estimation of Rs of $Co(OH)_2$/L-Asn, Co_2Ni-OH/L-Asn, CoNi-OH/L-Asn, $CoNi_2$-OH/L-Asn and $Ni(OH)_2$/L-Asn material as electrodes, and the values are 0.93, 0.66, 0.62, 0.59 and 0.45 Ω, respectively. The $CoNi_2$-OH/L-Asn has the lowest Rs than the other Co_xNi_{2-x}-OH/L-Asn electrodes, which can be attributed to the excellent structural properties.

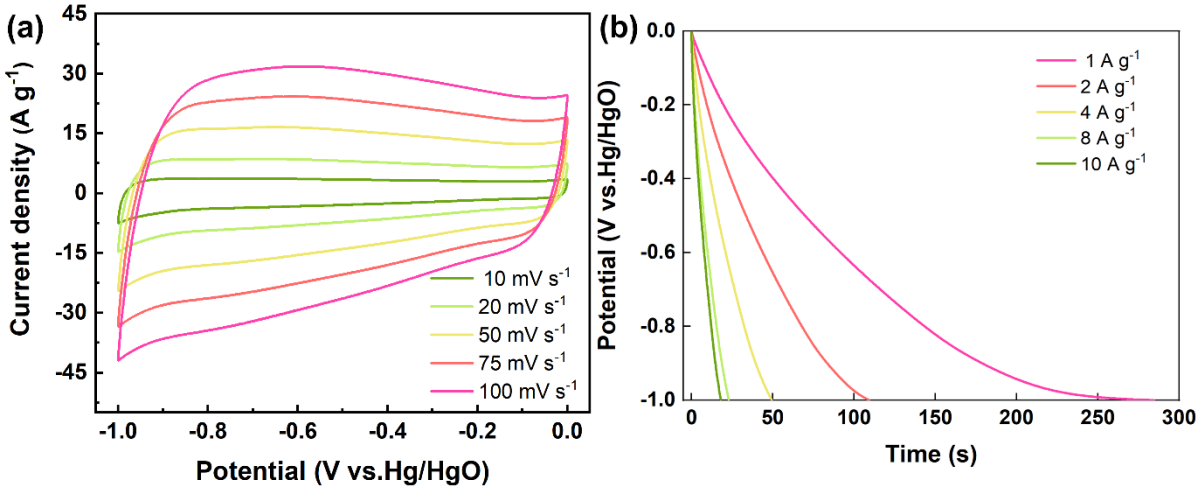

Figure S16. Cyclic voltammetry curves and galvanostatic discharge curves of N-rGO. (a) CV curves, (b) GCD curves

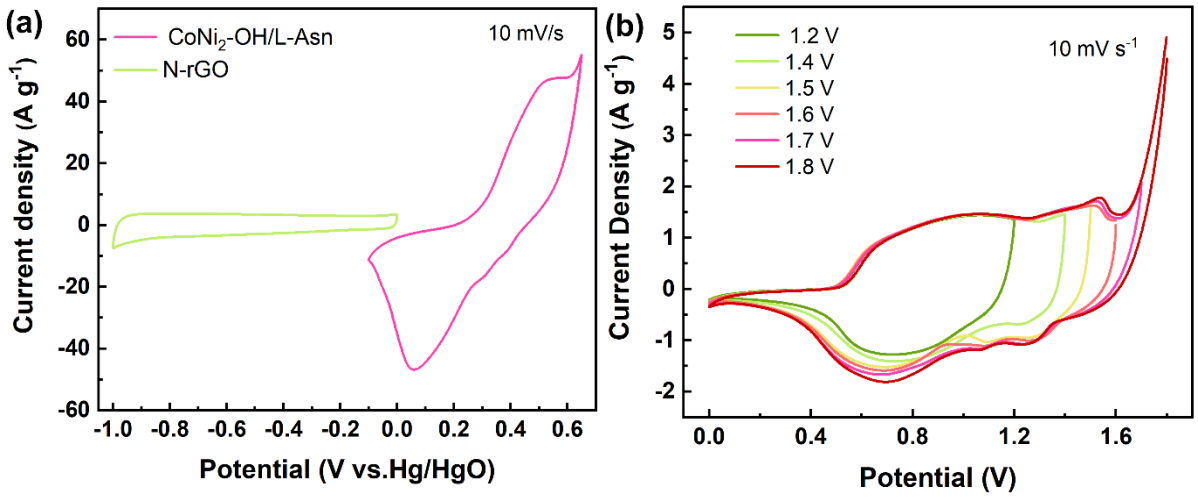

Figure S17. (a) CV curves for $CoNi_2$-OH/L-Asn and N-rGO. (b) CV curves of the $CoNi_2$-OH/L-Asn//N-rGO device obtained in different potential windows.

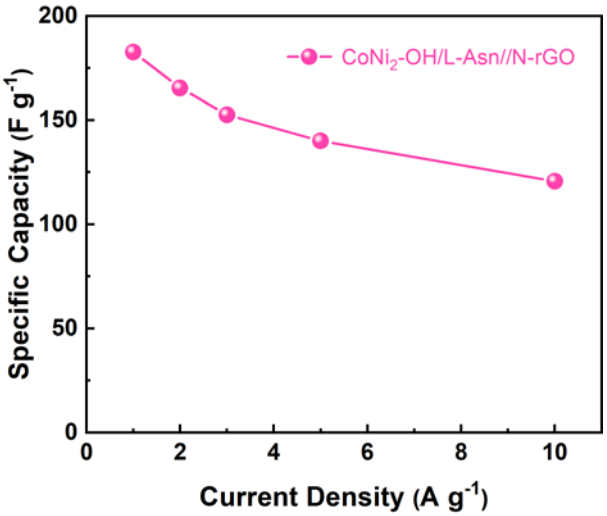

Figure S18. The specific capacity values of the $CoNi_2$-OH/L-Asn//N-rGO devices at different current densities.

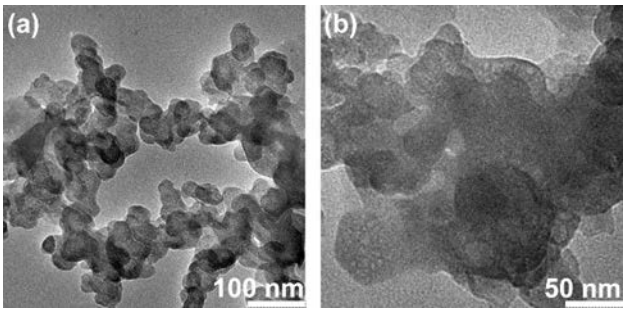

Figure S19. The TEM images of the electrode materials after 3000 cycles.

Table S2. Comparison of the electrochemical performance of ultrathin $CoNi_2$-OH/L-Asn electrode materials with the values in recent literature.

Device	Capacitance (F g^{-1})	Cycling number	Cycling retention	References
CC@$NiCo_2Al_x$-LDH	1137	10000 (5 A g^{-1})	100%	1[3]
CBC-N@LDH	1949.5	5000 (10 A g^{-1})	74.4%	2[4]
CNTs@NCDHNs	1823	~	~	4[5]
$NiCo_2S_4$	1036	2000 (5 A g^{-1})	87%	5[6]
LDHGOS	2246	1500 (20 mV s^{-1})	67	6[7]
NiCoP/NiCo-OH	1100	1000 (5 A g^{-1})	90%	7[8]
Ni/Co-LDH	1652	2000 (5 A g^{-1})	100%	8[2]
Co_3O_4@Co-MOF	1020	5000 (5 A g^{-1})	96.7%	9[9]
$CoNi_2$-OH/L-Asn	2608	3000 (5 A g-^{1})	100%	This work

Table S3. The electrochemical cycling stability of the asymmetric supercapacitors based on the $CoNi_2$-OH/L-Asn//N-rGO devices for recently reported ASC.

Device	Potential window (V)	Cycling number	Cycling retention	References
Ni-Co LDH//RGO	0-1.6	5000 (5 A g^{-1})	82 %	1[10]
Ni-Co LDH@rGO//rGO	0-1.5	4000 (5 A g^{-1})	80.2 %	2[11]
CoAlNi-LDH-NR//AC	0-1.6	3000 (2 A g^{-1})	82.2 %	3[12]
Ni/Co-N-350//PC	0-1.5	5000 (~)	82.4 %	4[13]
$NiCo_2S_4$//G/CS	0-1.6	10000 (5 A g^{-1})	78.6 %	5[6]
NSH//rGH	0-1.7	3000 (3 A g^{-1})	73.2 %	6[14]
Ni−$Co_{1.5}$−O//RGO@Fe_3O_4.	0-1.5	10000 (5 A g^{-1})	79.4 %	7[15]
$NiCo_2S_4$/NCF//OMC/NCF	0-1.7	10000 (7.4 A g^{-1})	70.4 %	8[16]
Ni/Co-LDHs//AC	0-1.6	1000 (100 mV s^{-1})	75.8 &	9[17]
$CoNi_2$-OH/L-Asn //N-rGO	0-1.6	5000 (10 A g^{-1})	82.4 %	This work

Table S4. Comparison of the energy density and power density of ultrathin $CoNi_2$-OH/L-Asn electrode with the values reported in recent literature.

Device	Energy density (Wh/kg)	Power density (W/kg)	References
CC@$NiCo_2Al_x$-LDH// ZPC	44	462	1[3]
$Ni_{0.7}Co_{0.3}(OH)_2$-0.2m-SH//AC	40.1	400.5	2[18]
NCH//rGH	44.4	460	3[14]
CBC-N@LDH//CBC-N	36.3	800.2	4[4]
$NiCo_2S_4$//G/CS	42.3	476	5[6]
Co-Ni-B-S/NF//AC/NF	50.0	857.7	6[19]
$Co_{0.2}Ni_{0.8}(OH)_2$//NGA	45.21	199.8	7[20]
$CoNi_2$-OH/L-Asn	64.9	799.9	This work

References

(1) Liu, Z.; Ma, R.; Osada, M.; Takada, K.; Sasaki, T., Selective and Controlled Synthesis of α- and β-Cobalt Hydroxides in Highly Developed Hexagonal Platelets. J. Am. Chem. Soc. **2005**, 127, 13869−13874.

(2) Li, S.; Zhang, Y.; Liu, N.; Yu, C.; Lee, S.-J.; Zhou, S.; Fu, R.; Yang, J.; Guo, W.; Huang, H.; Lee, J.-S.; Wang, C.; Kim, T. R.; Nordlund, D.; Pianetta, P.; Du, X.; Zhao, J.; Liu, Y.; Qiu, J., Operando Revealing Dynamic Reconstruction of NiCo Carbonate Hydroxide for High-Rate Energy Storage. Joule. **2020**, 4, 673−687.

(3) Gao, X.; Liu, X.; Wu, D.; Qian, B.; Kou, Z.; Pan, Z.; Pang, Y.; Miao, L.; Wang, J., Significant Role of Al in Ternary Layered Double Hydroxides for Enhancing Electrochemical Performance of Flexible Asymmetric Supercapacitor. Adv. Funct. Mater. **2019**, 29, 1903879.

(4) Lai, F.; Miao, Y.-E.; Zuo, L.; Lu, H.; Huang, Y.; Liu, T., Biomass-Derived Nitrogen-Doped Carbon Nanofiber Network: A Facile Template for Decoration of Ultrathin Nickel-Cobalt Layered Double Hydroxide Nanosheets as High-Performance Asymmetric Supercapacitor Electrode. Small. **2016**, 12, 3235−3244.

(5) Wang, Y.; Wei, H.; Lv, H.; Chen, Z.; Zhang, J.; Yan, X.; Lee, L.; Wang, Z. M.; Chueh, Y. L., Highly Stable Three-Dimensional Nickel-Cobalt Hydroxide Hierarchical Heterostructures Hybridized with Carbon Nanotubes for High-Performance Energy Storage Devices. ACS Nano. **2019**, 13, 11235−11248.

(6) Shen, L.; Yu, L.; Wu, H. B.; Yu, X. Y.; Zhang, X.; Lou, X. W., Formation of Nickel Cobalt Sulfide Ball-

in-Ball Hollow Spheres with Enhanced Electrochemical Pseudocapacitive Properties. Nat Commun. **2015**, 6, 6694.

(7) Chen, J.; Wang, X.; Wang, J.; Lee, P. S., Sulfidation of NiMn-Layered Double Hydroxides/Graphene Oxide Composites toward Supercapacitor Electrodes with Enhanced Performance. Adv. Energy Mater. **2016**, 6, 1501745.

(8) Li, X.; Wu, H.; Elshahawy, A. M.; Wang, L.; Pennycook, S. J.; Guan, C.; Wang, J., Cactus-Like NiCoP/NiCo-OH 3D Architecture with Tunable Composition for High-Performance Electrochemical Capacitors. Adv. Funct. Mater. **2018**, 28, 1800036

(9) Xu, Q.; Pang, H.; Xue, H.; Li, Q.; Zheng, S., A highly Alkaline-Stable Metal Oxide@Metal–Organic Framework Composite for High-Performance Electrochemical Energy Storage. Natl. Sci. Rev. **2020**, 7, 305−314.

(10) Chen, H.; Hu, L.; Chen, M.; Yan, Y.; Wu, L., Nickel-Cobalt Layered Double Hydroxide Nanosheets for High-Performance Supercapacitor Electrode Materials. Adv. Funct. Mater. **2014**, 24, 934−942.

(11) Karthik Kiran, S.; Shukla, S.; Struck, A.; Saxena, S., Surface Engineering of Graphene Oxide Shells Using Lamellar LDH Nanostructures. ACS Appl. Mater. Interfaces. **2019**, 11, 20232-20240.

(12) Chen, H.; Zhang, H.; Zhang, Y.; Wang, Y.; Su, X.; Zhang, L.; Lin, Z., General Strategy toward Hexagonal Ring-Like Layered Double Hydroxides and Their Application for Asymmetric Supercapacitors. Chem. Eng. J. **2019**, 375, 121926

(13) Liu, X.; Zang, W.; Guan, C.; Zhang, L.; Qian, Y.; Elshahawy, A. M.; Zhao, D.; Pennycook, S. J.; Wang, J., Ni-Doped Cobalt–Cobalt Nitride Heterostructure Arrays for High-Power Supercapacitors. ACS Energy Letters. **2018**, 3, 2462−2469.

(14) Wen, F.; Zhang, Y.; Qian, X.; Zhang, J.; Hu, R.; Hu, X.; Wang, X.; Zhu, J., Carbon-Induced Generation of Hierarchical Structured $Ni_{0.75}Co_{0.25}(CO_3)_{0.125}(OH)_2$ for Enhanced Supercapacitor Performance. ACS Appl. Mater. Interfaces. **2017**, 9, 44441−44451.

(15) Li, X.; Wang, L.; Shi, J.; Du, N.; He, G., Multishelled Nickel–Cobalt Oxide Hollow Microspheres with Optimized Compositions and Shell Porosity for High-Performance Pseudocapacitors. ACS Appl. Mater. Interfaces. **2016**, 8, 17276−17283.

(16) Shen, L.; Wang, J.; Xu, G.; Li, H.; Dou, H.; Zhang, X., $NiCo_2S4$Nanosheets Grown on Nitrogen-Doped Carbon Foams as an Advanced Electrode for Supercapacitors. Adv. Energy Mater. **2015**, 5, 1400977.

(17) Li, T.; Li, G. H.; Li, L. H.; Liu, L.; Xu, Y.; Ding, H. Y.; Zhang, T., Large-Scale Self-Assembly of 3D Flower-Like Hierarchical Ni/Co-LDHs Microspheres for High-Performance Flexible Asymmetric

Supercapacitors. ACS Appl. Mater. Interfaces. **2016**, 8, 2562−2572.

(18) Zhang, H.; Xu, B.; Mei, H.; Mei, Y.; Zhang, S.; Yang, Z.; Xiao, Z.; Kang, W.; Sun, D., "HOT" Alkaline Hydrolysis of Amorphous MOF Microspheres to Produce Ultrastable Bimetal Hydroxide Electrode with Boosted Cycling Stability. Small. **2019**, 15, 1904663.

(19) Wang, Q.; Luo, Y.; Hou, R.; Zaman, S.; Qi, K.; Liu, H.; Park, H. S.; Xia, B. Y., Redox Tuning in Crystalline and Electronic Structure of Bimetal-Organic Frameworks Derived Cobalt/Nickel Boride/Sulfide for Boosted Faradaic Capacitance. Adv. Mater. **2019**, 31, e1905744.

(20) Cao, J.; Mei, Q.; Wu, R.; Wang, W., Flower-Like Nickel–Cobalt Layered Hydroxide Nanostructures for Superlong-Life Asymmetrical Supercapacitors. Electrochimica Acta. **2019**, 321, 134711.